Case Studies in Thermal Engineering 59 (2024) 104596

Contents lists available at ScienceDirect

Case Studies in Thermal Engineering

journal homepage: www.elsevier.com/locate/csite

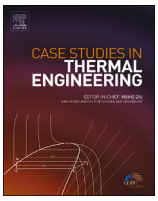

Effects of temperature uniformity and nonuniformity on thermoelectric generator performance across hot and cold sides

Abdelkader Rjafallah *, Abubaker Younis, Daniel Tudor Cotfas, Petru Adrian Cotfas

Electrical Engineering and Computer Science Faculty, Transilvania University of Brasov, 500036, Brasov, Romania

ARTICLE INFO

Keywords:
Solar thermoelectric generator
Uniform temperature distribution
Nonuniform temperature distribution
Numerical 3D simulation
Comsol multiphysics

ABSTRACT

Solar Thermoelectric Generators (STEG) are gaining attention for clean energy but face nonuniform temperature distribution due to optical concentrators and heat sinks. While prior studies used central circles or identical squares to represent temperature variations, this paper examines six circular and rectangular patterns. Using COMSOL, the TEG module was simulated under four boundary conditions: (1) uniform temperatures on both sides, (2) six patterns on the hot side, (3) six patterns on the cold side, and (4) six patterns on both sides for the first time. Experimentally, the I–V and P–V characteristics of STEG were measured using the capacitor technique for four concentration ratios (20, 40, 60, and 80 suns) obtained using the KIRAN-42 simulator. Simulations aligned well with all experiments under condition (1). The 3rd circular and rectangular pattern matched 11 times, while the 1st pattern matched once under conditions (2) – (4). The Root Mean Square Error (RMSE) between the measured and simulated P_{max}, based on average measured temperatures, was 0.505. For condition (1), the RMSE was 0.017, while for conditions (2) – (4), it was 0.027 (0.033), 0.031 (0.031), and 0.044 (0.047) for the 3rd circular (rectangular) pattern, respectively. These findings indicate improved alignment between experiments and simulations.

1. Introduction

Today, the generation of energy from renewable energy sources (RES) holds significant importance for humanity as it replaces the use of fossil energy sources [1]. RES offer the advantages of being virtually inexhaustible and producing minimal pollution, but they are characterized by intermittency and relatively high upfront costs [2]. Consequently, both the research community and the industry are dedicated to finding new RES solutions and enhancing the performance of existing ones [3]. According to the REN21 report [4], the European Union (EU) has set a target of sourcing at least 32 % of its energy from RES by 2030. One promising avenue for improving the efficiency of RES involves the hybridization of technologies [5]. Various solutions for implementing RES hybridization exist, each with its own set of advantages and disadvantages [6].

Thermoelectric generators (TEGs) are devices that directly convert thermal energy into electricity based on the Seebeck effect [7]. TEGs find applications in various areas due to their ability to generate direct current as long as there is a temperature difference between their hot and cold sides [8]. Additionally, TEGs offer several advantages, such as direct energy conversion, the absence of moving components, a long lifespan, stability, noiseless modularity, no pollution, and scalability [9]. However, the widespread use of TEGs has been limited by their high module cost and relatively low efficiency [10].

* Corresponding author.
E-mail address: abdelkader.rjafallah@unitbv.ro (A. Rjafallah).

https://doi.org/10.1016/j.csite.2024.104596
Received 6 March 2024; Received in revised form 5 May 2024; Accepted 21 May 2024
Available online 22 May 2024

Currently, the focus of research and industry has become increasingly attractive on TEGs to reduce their module prices by exploring more affordable and eco-friendly materials [11]. This growing interest is evident from numerous review papers published in the last five years, covering topics ranging from TEGs as individual components to their role in photovoltaic and TEG (PV-TEG) hybrid systems [12]. These papers explore various aspects, including TEG technologies, materials, and applications [10,13], optimization of TEG structure and geometry [10,14], experimental studies to enhance the thermoelectric figure-of-merit [15], thermal configurations for solar applications [16–18], and methods for improving PV or hybrid system performance through the integration of TEGs, including hybrid systems like concentrated PV and TEG (CPV-TEG) [19,20].

On the other hand, solar energy, as a clean and abundant source, can be utilized as a heat source for TEGs [21]. However, the challenge lies in the low heat flux incident on the hot side (HS) of TEGs when directly utilizing solar light [22]. Fortunately, optical concentrators, such as optical lenses or mirrors, are commonly employed to concentrate sunlight onto the hot side of TEGs, enhancing the input heat flux [23]. Concentrating Solar Thermoelectric Generators (STEGs) represent a specific implementation of this concept and characterized by their ability to use concentrated sunlight, significantly increasing electricity production efficiency [24]. Nevertheless, these optical concentrators result in nonuniform solar radiation on the hot side of STEGs, regardless of the type of optical concentrators used [22].

Numerous papers have explored TEGs and STEGs, investigating the physical properties of thermoelectric materials, the geometry of thermoelectric legs [25–33], manufacturing techniques of thermoelectric modules [34], and temperature distribution uniformity on the hot and/or cold sides of thermoelectric modules [35,36]. In contrast, few papers have focused on the effect of temperature distribution nonuniformity on the hot and/or cold sides of thermoelectric modules [22,24,37–43]. Moreover, minimal research has been conducted to investigate the effects of both uniform and nonuniform temperature distribution patterns on the hot and cold sides separately and together in the same study. Additionally, nonuniform temperature distribution patterns are crucial as they accurately reflect the diverse and realistic temperature distributions encountered in real-world scenarios.

Admasu et al. [39] numerically and experimentally investigated the effects of temperature uniformity and nonuniformity on the outputs of a TEG module. They divided the hot side surface into four squares while maintaining a uniform temperature on the cold side. Their findings indicated that a uniform temperature distribution across the hot side results in higher outputs compared to a nonuniform distribution. Pfeiffelmann et al. [42] tested the performance of a TEG module with uniform temperature distribution on the hot side and nonuniform distribution in one spatial direction on the cold side, where the cold side is divided into two rectangles. They observed that with a temperature variation of 8 % of the temperature difference between the hot and cold sides, the TEG performance exhibited only a small difference compared to a uniform distribution. Lashin et al. [37] conducted simulations on the electrical and thermal performance of three TEG modules with different areas under partial illumination at two light intensities: 12 × and 105 × Sun on the hot side, while maintaining a constant temperature on the cold side. They simulated the concentrated partial illumination on the hot side using a central cercle, ranging from 10 % to 80 %. The electrical performance of the TEG modules exhibited distinct behavior under each intensity. Pfeiffelmann et al. [41] again experimentally and numerically analyzed the performance of a TEG module with a nonuniform distribution in one spatial direction on the cold side, while maintaining a uniform temperature on the hot side. This one-dimensional nonuniform distribution was achieved by using four identical cooling copper blocks, with two blocks having a higher temperature than the other two. They also found a negligible effect of temperature nonuniformity compared to a uniform distribution. A numerical study was conducted by Ge et al. [24] to investigate the impact of both nonuniform and uniform heat flux inputs on the hot side on STEG performance. The hot-side surface was divided into a grid of 20 × 20 squares, each measuring 2 mm × 2 mm. These squares were grouped into 10 regions with varying heat flux levels, gradually decreasing from the center to the periphery, simulating nonuniform irradiation intensity. Results demonstrated that with increased unevenness in heat flux, the center temperature gradually rose, leading to a 3.8 % reduction in output power when the maximum temperature difference on the hot side surface was 46.2 K. However, these previous studies used either one central cercle with different radii or identical squares with same dimensions to represent temperature nonuniformity on either the hot-side or cold-side surfaces. Additionally, representing nonuniform temperature distribution with these patterns does not accurately reflect the diverse and realistic temperature distributions encountered in real-world scenarios.

The objective of this paper is to address a significant gap in existing research by conducting a comprehensive study on two types of patterns: circular and rectangular, for nonuniform temperature distribution across both the hot and cold sides of TEGs. Unlike previous studies that have primarily focused on using either one central cercle with different diameters or identical squares with the same dimensions to simulate nonuniform temperature distributions on either the hot side or cold side surfaces, our investigation explores six different circular and rectangular patterns of nonuniform temperature distributions on both the hot and cold sides of a TEG module, in addition to uniform distribution. The TEG module was simulated under four distinct boundary conditions: (1) uniform temperature distributions on both the hot and cold sides, (2) six circular and rectangular patterns of nonuniform temperature distribution on the hot side with uniform temperature distribution on the cold side, (3) uniform temperature distribution on the hot side with six circular and rectangular patterns of nonuniform temperature distribution on the cold side, and (4) six circular and rectangular patterns of nonuniform temperature distribution on both the hot and cold sides. This approach provides novel insights into the effects of nonuniform temperature distribution patterns on TEG module performance, offering valuable contributions to the field of thermoelectric energy conversion.

Therefore, the rest of the article comes as follows: Section 2 describes the materials and methodology used for simulating the STEG module for each boundary condition and the experiment setup used. This involves constructing numerical three-dimensional models using Comsol Multiphysics Software based on the Finite Element Method (FEM). The governing equations used in COMSOL Multiphysics are also presented. Section 3 outlines results obtained by simulations and experimentations. Simulation results provided by

the TEG module under each case considered for each boundary condition are analyzed, discussed, and compared with the experimental results. Section 4 presents the conclusions drawn from this investigation and proposes some perspectives for future research.

2. Materials and methods

2.1. Thermoelectric generator

The thermoelectric generator analyzed through simulation and experimentation is TEC1-12706 module, which is based on bismuth telluride (Bi_2Te_3) semiconductor material. This commercially available module is designed for low-temperature applications below 250 °C, offering a combination of affordability, high performance, and practicality. Bi_2Te_3 compound is the standard thermoelectric material and exhibits the highest figure of merit within this temperature range.

Furthermore, it serves as the predominant material utilized in commercial thermoelectric modules, such as the TEC1-12706 module employed in our experiments. The thermoelectric module utilized in this study measures 40 mm × 40 mm × 3.8 mm in size and consists of 127 p-n pairs with rectangular-shaped legs made of Bi_2Te_3 semiconductor material, each measuring 1.4 mm × 1.4 mm × 2.2 mm. Additionally, the module features two alumina ceramic layers on the top and bottom, along with 255 copper conductors, as detailed in Table 1. The model considered constant material properties for Bi_2Te_3 because all the simulations conducted in this study had an average applied temperature ($T_{av} = T_h - T_c$) ranging between 21 °C and 64 °C. According to the material properties for Bi_2Te_3 available in the COMSOL Multiphysics materials library (refer to Table 2) [44], the corresponding material properties for this temperature range are: 210×10^{-6} (V/K) ≤ S ≤ 225×10^{-6} (V/K), κ = 1.6 (W/(m × K)), and 0.71×10^5 (S/m) ≤ σ ≤ 0.87×10^5 (S/m). Therefore, the optimized material properties for Bi_2Te_3 in this study and material properties for alumina ceramic layers and copper conductors are detailed in Table 3.

2.2. Assumptions and boundary conditions

To analyze the performance of the TEG module under the four boundary conditions, the modeling was conducted considering the following assumptions and boundary conditions.

- The TEG module is analyzed using the following Physics Interfaces: Heat Transfer, Electric Currents, and Electrical Circuit.

Table 1
Geometric dimensions of TEG module used in simulation.

Name	Dimensions (mm)	Description
TEG length	40	Total TEG length
TEG width	40	Total TEG width
TEG height	3.8	Total TEG height
Ceramic length	40	Ceramics length
Ceramic width	40	Ceramics width
Ceramic height	0.7	Ceramics thickness
Copper height	0.1	Coppers thickness
Leg height	2.2	Legs height
Leg length	1.4	Legs length
Leg width	1.4	Legs width
Pitch	1	Distance between legs
PN	127	Number of thermocouples

Table 2
Temperature dependent material properties of Bi_2Te_3 from the COMSOL Multiphysics materials library [44].

Temperature T (°C)	Seebeck Coefficient S (V/K)	Thermal Conductivity κ (W/(m × K))	Electrical Conductivity σ (S/m)
−73	168×10^{-6}	2.4	1.43×10^5
−23	192×10^{-6}	1.9	1.11×10^5
+27	210×10^{-6}	1.6	0.87×10^5
+77	225×10^{-6}	1.6	0.71×10^5
+127	237×10^{-6}	1.75	0.59×10^5

Table 3
Material properties used in simulation [44].

Materials	Thermal Conductivity κ (W/(m × K))	Electrical Conductivity σ (S/m)	Specific Heat Capacity C_p (J/(kg × K))	Density ρ (kg/m^3)	Relative Permittivity ε	Seebeck Coefficient S (V/K)
Ceramic	27	–	900	3900	–	0
Copper	400	599.8×10^5	385	8940	1	6.5×10^{-6}
Bi_2Te_3						
- p-type	1.6	1.25×10^5	154	6800	1	$+210 \times 10^{-6}$
- n-type	1.6	1.25×10^5	154	6800	1	-210×10^{-6}

- The TEG module is studied in steady-state.
- The TEG module is assumed to be isolated; the air surrounding it is not considered.
- Heat losses in the TEG module are neglected.
- The alumina ceramics, copper conductors, and p-n pairs in the TEG module are treated as three different homogenous substances with associated isotropic and constant thermophysical properties.
- The p-n pairs are composed of bismuth telluride (Bi_2Te_3).
- The thermoelectric properties of the p-n pairs, such as the Seebeck coefficient, thermal conductivity, and electrical conductivity, are assumed to be constant.
- Uniform and nonuniform patterns of temperature distributions are applied on the hot and cold sides of the TEG module.

2.3. Theoretical aspects

The short-circuit current (I_{sc}), open-circuit voltage (V_{oc}), and maximum power (P_{max}) provided by the TEG module were analyzed under four distinct boundary conditions: (1) uniform temperatures over both the hot and cold sides, (2) six circular and rectangular patterns of nonuniform temperature distribution over the hot side with uniform temperature over the cold side, (3) uniform temperature over the hot side with six circular and rectangular patterns of nonuniform temperature distribution over the cold side, and (4) six circular and rectangular patterns of nonuniform temperature distribution over both the hot and cold sides. COMSOL Multiphysics software, which is based on Finite Element Method (FEM), was utilized to simulate the thermoelectric behavior of STEG modules under these boundary conditions as well as simulation results were compared with experimental data.

In the first step, a three-dimensional model of TEG module is used, which was constructed in COMSOL Multiphysics software and was validated in our previous published study [10] to simulate the thermoelectric behavior of TEG module under the boundary conditions above. In the second step, we slightly adjusted our three-dimensional model to suit our study discussed in the present paper. (see Fig. 1). In the last step, the experimental data is compared with the simulation results provided by the TEG module under the boundary conditions mentioned above in terms of short-circuit current (I_{sc}), open-circuit voltage (V_{oc}), and maximum power (P_{max}).

The general equations used in the simulation by COMSOL Multiphysics, considering all material properties of the TEG module to be isotropic, are [36,45].

- For conservation of heat energy in immobile solid [38]:

$$\rho C_p \frac{\partial T}{\partial t} + \nabla \bullet \boldsymbol{q} = Q \tag{1}$$

Where ρ is the density (kg/m^3), C_p the heat capacity at constant pressure (J/(kg • K)), Q the Joule heat source (W/m^3) given by Eq. (2), T the temperature (K), and $\boldsymbol{q}$ is the conductive heat flux vector (W/m^2) given by Eq. (3).

$$Q = \boldsymbol{J} \bullet \boldsymbol{E} \tag{2}$$

$$\boldsymbol{q} = -k\nabla T + \boldsymbol{q_p} \tag{3}$$

Where $\boldsymbol{J}$ is the electric current density vector (A/m^2) given by Eq. (5), $\boldsymbol{E}$ the electric field vector (V/m), k the thermal conductivity (W/(m • K)), and $\boldsymbol{q_p}$ is the power vector (W/m^2).

- For conservation of electrical current in immobile solid [38,46,47]:

$$\nabla \bullet \boldsymbol{J} = Q_{j,v} = \nabla \bullet \left[\varepsilon \nabla \frac{\partial V}{\partial t}\right] \tag{4}$$

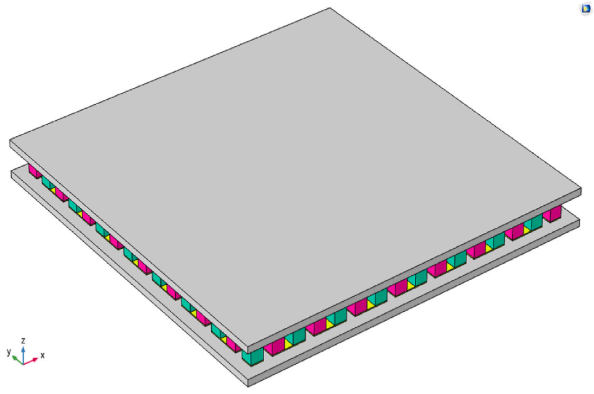

Fig. 1. Simulation of a TEG module using COMSOL Multiphysics software. The module includes 2 alumina ceramics, 255 copper conductors, and 127 p-n pairs with rectangular-shaped legs made of Bi_2Te_3 semiconductor material, each measuring 1.4 mm × 1.4 mm × 2.2 mm.

$$\boldsymbol{J} = \sigma \boldsymbol{E} + \boldsymbol{J_e} \tag{5}$$

$$\boldsymbol{E} = -\nabla V \tag{6}$$

where $Q_{j,v}$ is the current source (A/m^3), σ the electrical conductivity (S/m), $\boldsymbol{J_e}$ the external current density vector (A/m^2) given by Eq. (9), and V is the electric scalar potential (V).

- For thermoelectric effects in immobile solids [10]:

$$P = ST \tag{7}$$

$$\boldsymbol{q_p} = P\boldsymbol{J} \tag{8}$$

$$\boldsymbol{J_e} = -\sigma S \nabla T \tag{9}$$

where P is the Peltier coefficient (V), S the Seebeck coefficient (V/K).

Substituting Eqs. (2), (3) and (5)–(9) in Eqs. (1) and (4) produce a system of coupled equations of thermoelectricity as follows [38]:

$$\rho C_p \frac{\partial T}{\partial t} - \nabla \bullet [\sigma S T \nabla V] - \nabla \bullet \left[\sigma S^2 T \nabla T\right] - \nabla \bullet [k \nabla T] - \sigma \nabla V \bullet \nabla V - \sigma S \nabla T \bullet \nabla V = 0 \tag{10}$$

$$\nabla \bullet [\sigma \nabla V] + \nabla \bullet [\sigma S \nabla T] + \nabla \bullet \left[\varepsilon \nabla \frac{\partial V}{\partial t}\right] = 0 \tag{11}$$

In a steady state thermoelectric analysis, thermal and electrical loads do not vary over time. In the present steady state model, the coupled equations of thermoelectricity can be rewritten as follows [48]:

$$\nabla \bullet [\sigma S T \nabla V] + \nabla \bullet \left[\sigma S^2 T \nabla T\right] + \nabla \bullet [k \nabla T] + \sigma \nabla V \bullet \nabla V + \sigma S \nabla T \bullet \nabla V = 0 \tag{12}$$

$$\nabla \bullet [\sigma \nabla V] + \nabla \bullet [\sigma S \nabla T] = 0 \tag{13}$$

The V_{oc} generated by the thermoelectric generator when a temperature difference between the hot and cold sides is present (see Fig. 2a) and is given by Ref. [33]:

$$V_{oc} = S \Delta T \tag{14}$$

$$\Delta T = \left(T_h - T_c\right) \tag{15}$$

where T_h is the hot-side temperature, and T_c is the cold-side temperature.

The heat absorbed at the hot side Q_h and heat rejected from the cold side Q_c of the thermoelectric generator connected in series to electrical resistance R_L (see Fig. 2b) are [36]:

$$Q_h = SIT_h - \frac{1}{2}\left(R_{in} I^2\right) + K\left(T_h - T_c\right) \tag{16}$$

$$Q_c = SIT_c - \frac{1}{2}\left(R_{in} I^2\right) + K\left(T_h - T_c\right) \tag{17}$$

Where S, R_{in}, and K are the total Seebeck coefficient (as defined in Eq. (18)), total internal resistance (as defined in Eq. (19)), and total thermal conductance (as defined in Eq. (20)) of p-n pairs, respectively, and I is the electric current flowing across the load resistance R_L (as defined in Eq. (23)).

$$S = N\left(S_p - S_n\right) \tag{18}$$

$$R_{in} = N\left(\frac{\rho_p L_p}{A_p} + \frac{\rho_n L_n}{A_n}\right) \tag{19}$$

$$K = N\left(\frac{k_p A_p}{L_p} + \frac{k_n A_n}{L_n}\right) \tag{20}$$

Where N is the total number of p-n pairs, S_p is the p-type legs Seebeck coefficient, S_n the n-type legs Seebeck coefficient, ρ_p the p-type legs electrical resistivity, ρ_n the n-type legs electrical resistivity, k_p the p-type legs thermal conductivity, k_n the n-type legs thermal conductivity, A_p the p-type legs cross-sectional area, A_n the n-type legs cross-sectional area, L_p the p-type legs length, and L_n is the n-type legs length.

The electric resistance of the copper electrodes was not included in the total internal resistance R_{in} of the TEG module for two reasons. Firstly, the electric resistance of the copper electrodes is very negligible compared to the electric resistance of n-type and p-type legs. According to Table 3, the electrical conductivity of the copper conductors is greater than that of n-type and p-type legs by 480

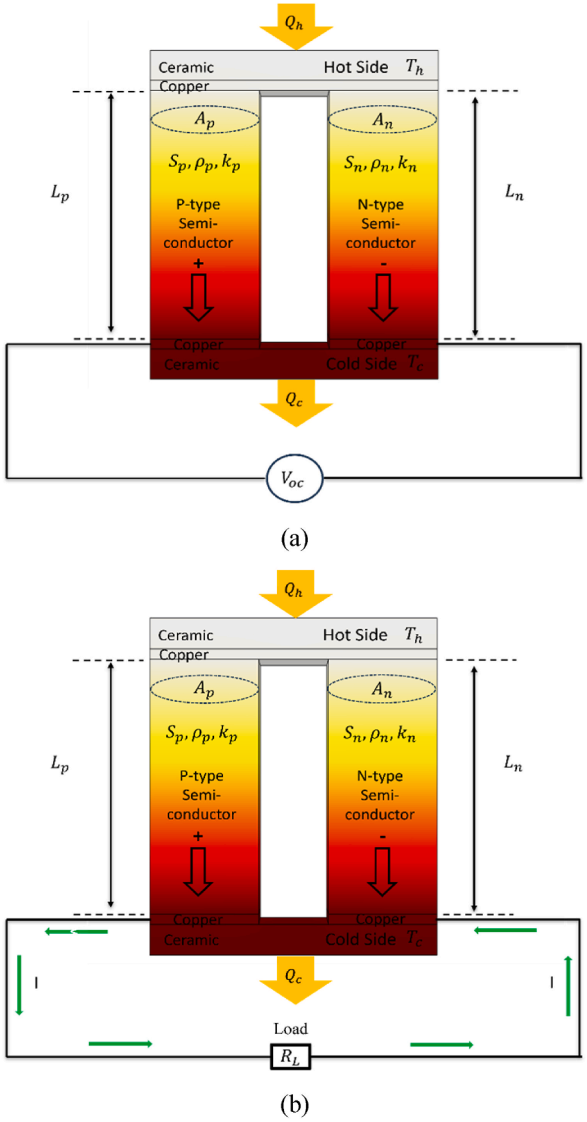

Fig. 2. Schematic diagrams of thermoelectric generator depicting a) open-circuit condition and b) under load [36].

times, therefore, inversely, their electrical resistivity is much lower compared to resistivity of n-type and p-type legs. Secondly, the electric resistance of the copper electrodes was omitted in the calculations for simplification purposes.

By applying the first law of thermodynamics, the electric power P_{out} generated by the thermoelectric generator across the load resistance R_L is given by Ref. [36]:

$$P_{out} = Q_h - Q_c = SI\left(T_h - T_c\right) - R_{in}I^2 \tag{21}$$

Moreover, the voltage V can be deduced as,

$$V = R_L I = S\left(T_h - T_c\right) - R_{in}I \tag{22}$$

Therefore, the electric current I can be written as,

$$I = \frac{V}{R_L} = \frac{S\left(T_h - T_c\right)}{R_{in} + R_L} \tag{23}$$

Hence, the electric power P_{out} can be rewritten as,

$$P_{out} = R_L I^2 = R_L \left(\frac{S\Delta T}{R_{in} + R_L} \right)^2 \tag{24}$$

The maximum power $P_{out,max}$ generated by the TEG module across the load resistance R_L is obtained when $R_L = R_{in}$.

$$P_{out,max} = \frac{1}{4} \frac{(S\Delta T)^2}{R_L} \tag{25}$$

2.4. Grid-independent analysis

A finite element-based approach was employed to solve the governing equations of the model using the COMSOL Multiphysics 5.5 software. The study conducted a mesh sensitivity analysis to explore the influence of mesh size on model output, utilizing three different mesh sizes that were progressively refined. Each mesh size was analyzed under uniform temperatures on the hot and cold sides ($T_h = 62\ ^\circ C - T_c = 20\ ^\circ C$). Free Tetrahedral meshing, a technique that generates tetrahedra elements without constraints on size or shape, was utilized in our finite element analysis-based computational simulations. Unlike structured meshes, which have a regular and structured arrangement of elements, free tetrahedral meshing offers greater flexibility in capturing complex geometries and can adapt to irregular shapes or regions with varying material properties. This flexibility makes free tetrahedral meshing well-suitable for modeling complex structures and phenomena in various engineering and scientific fields. Table 4 presents the I_{sc}, V_{oc}, and P_{max} generated by the TEG module for the three different mesh sizes. The study revealed that as the mesh size becomes finer, there is no significant change observed in I_{sc}, V_{oc}, and P_{max}. Therefore, the element size "Normal" was selected for the simulations, as it balances computation time and resource compatibility. Fig. 3 illustrates the mesh generated using the Free Tetrahedral meshing technique.

2.5. Experimental setup

The experiments were conducted at the IMDEA Energy Institute in Madrid, Spain, using a High Flux Solar Simulator. The experimental setup utilized a single lamp of the solar simulator, as depicted in Fig. 4a. Variations in irradiance were achieved by adjusting the position of the table support, which can be moved in three directions. The improved TEG, specifically the TEC1-12706 model, featuring a directly deposited absorbent layer, was employed in the experiments [11]. The mounting system of the TEG and the locations of the two K-type thermocouples, with an accuracy of $\pm 1.5\ ^\circ C$, used to measure the temperature of the hot side are illustrated in Fig. 4b. To maintain the integrity of the measurement system and prevent degradation, the TEG was enclosed within an alumina sheet. The I–V characteristics of the TEG were measured using a developed measurement system based on the capacitor technique and the NI cRIO 9074 platform based on a 400 MHz processor and an FPGA Spartan-3 chip [49] at four concentration ration from 20 to 80 suns with a 20 suns step. The cooling system utilized water, which was maintained at a quasi-constant temperature using a chiller, as shown in Fig. 4a. The temperature of the cold side of the thermoelectric generator was monitored using two additional K-type thermocouples, with the same level of accuracy. The TEG was firmly secured using two screws to ensure excellent thermal contact with the cooler, which was an aluminum block. Furthermore, a thermoconductive paste based on silver with 6 W/(m × K) thermal conductivity coefficient was placed between the TEG and the cooler to enhance heat transfer efficiency.

Table 4
Results of the TEG module for mesh sensibility study.

Element Size	Element Number	I_{sc} (A)	V_{oc} (V)	P_{max} (W)
Normal	285,887	0.8858	2.1316	0.5090
Fine	545,780	0.8854	2.1310	0.5087
Finer	2,618,547	0.8849	2.1304	0.5082

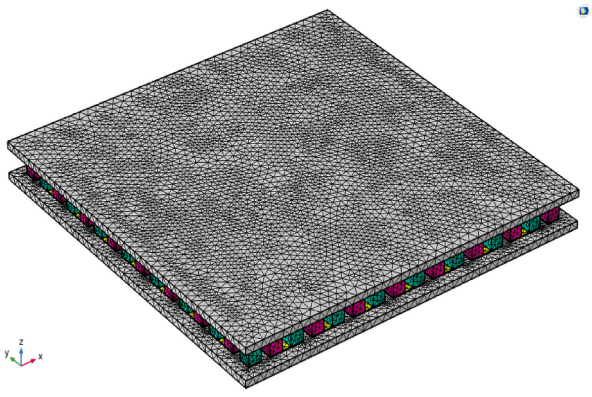

Fig. 3. Mesh generated using the Free Tetrahedral meshing technique.

Fig. 4. a) Experimental setup with the illumination lamp; b) Placement of the TEG.

3. Results and discussion

3.1. Experimental results

In this experiment, four levels of concentrated light were considered. Due to the asymmetry in flux distribution [50] and the need to achieve a small concentration ratio ranging from 10 suns to 100 suns, the flux does not fall perpendicular to the thermoelectric generator. As a result, the hot side of the TEG is not uniformly illuminated, leading to non-uniform temperature distribution on the hot side. The commercial TEC1-12706 module, enhanced with the absorbent layer, was subjected to testing. The I–V characteristics of the TEG module were measured at each concentration ratio, and corresponding P–V characteristics were calculated (i.e., Exp. (1)–(4)). The results obtained from measurements, including I_{sc}, V_{oc}, and P_{max} generated by the TEC1-12706 module under four concentration ratios, are presented in Table 5.

The temperatures on the hot and cold sides of the TEG module, measured with those four thermocouples, are presented in Table 5. There are differences in temperature measured with the two thermocouples for the hot side and also for the cold side. The temperature differences are higher for the hot side of the TEG, while a smaller temperature difference is detected on the cold side surface. Examining these results, as well as other scenarios, underscores the importance of investigating the behavior of the thermoelectric generator concerning varying degrees of temperature distribution non-uniformity on both the hot and cold sides of the TEGs.

3.2. Simulation results

The objective is to examine both uniform temperature distribution and six circular and rectangular patterns of non-uniform temperature distribution on either the hot or cold side of the TEG module, as depicted in Fig. 1. Table 1 provides the geometric dimensions used in the simulation for our TEG module, which features a constant cross-sectional area of 1.4 mm × 1.4 mm and rectangular-shaped legs.

3.2.1. Case 1: uniform temperatures over hot and cold sides

In the first step of the simulation (Case 1), the average temperatures measured on both the hot side (HS) and cold side (CS) surfaces were applied. If the simulations aligned with the experimental results, the same average temperatures were used for subsequent simulations in Cases 2–4. However, if the simulations did not match the experiments, adjustments were made to the average temperatures on the hot side surface. These adjustments involved varying the average temperatures within the range of minimum to maximum measured temperatures on the hot side surface until the simulations matched the experimental data. Given the significant temperature nonuniformity observed on the hot side surface, adjustments were focused exclusively on the average temperatures on the hot side. However, due to the pronounced temperature nonuniformity on the hot side, the average temperatures calculated in Table 5 did not accurately reflect the actual average temperatures, especially when simulations did not match the experimental results.

According to Table 5, the average temperatures of the measured temperatures in Exp. (1) were 62 °C and 20 °C for hot and cold sides, respectively. In the simulation of Case 1, these average temperatures were initially applied, but the simulation did not match Exp. (1). Consequently, alternative average temperature values within the measured temperature range ($T_h(1)$ = 54.2 °C and $T_h(2)$ = 70.7 °C) were applied on the hot side. To make the text more concise, simulations for specific average temperatures were pre-

Table 5
HS and CS temperatures, I_{sc}, V_{oc}, and P_{max} for the commercial TEC1-12706 module under four different concentration ratios.

Experiments	$T_h(1)$ (°C)	$T_h(2)$ (°C)	$T_{h,av}$ (°C)	$T_c(1)$ (°C)	$T_c(2)$ (°C)	$T_{c,av}$ (°C)	I_{sc} (A)	V_{oc} (V)	P_{max} (W)
Exp. (1)	54.2	70.7	62.4	20.2	19.6	19.9	0.926	2.386	0.555
Exp. (2)	92.1	126.4	109.2	30.1	30.6	30.3	1.539	4.690	1.807
Exp. (3)	128.1	175.6	151.8	39.9	42.5	41.2	1.903	6.490	3.088
Exp. (4)	151.4	205.5	178.4	47.2	52.0	49.6	2.081	7.274	3.776

sented, specifically T_h = 62 °C, 63 °C, 64 °C, and 65 °C to determine the most effective average temperature that aligned with Exp. (1). Fig. 5 illustrates one simulation from this set, conducted with the mentioned average temperatures, where the TEG module maintained a constant HS temperature of 64 °C and a constant CS temperature of 20 °C.

Fig. 6 depicts the temperature variation across the TEG module, which linearly varies along the height of the n-type and p-type legs but remains constant along the height of the ceramic plates and copper sheets.

Fig. 7 and Table 6 present the corresponding results derived from simulations. After comparing these simulations with Exp. (1), we found that the closest match occurred with an HS average temperature of 64 °C. This indicates that in the actual scenario of Exp. (1), the HS temperature exhibited nonuniformity, and the HS average temperature was determined to be 64 °C instead of 62 °C. Consequently, we adopted this HS average temperature of 64 °C for simulating Cases 2–4. Similarly, for other experiments, the HS average temperatures determined by simulations were 109 °C for Exp. (2), 145 °C for Exp. (3), and 165 °C for Exp. (4) (see Table 6).

Upon comparison with Exp. (1), the simulation showed that under T_h = 64 °C – T_c = 20 °C, I_{sc} and P_{max} provided by the TEG module were 0.2 % and 0.7 % higher, respectively, while V_{oc} was 6.4 % lower. Similarly, compared to Exp. (2), the simulation demonstrated an 8.0 % higher I_{sc} under T_h = 109 °C – T_c = 30 °C, while V_{oc} and P_{max} were 14.5 % and 0.5 % lower, respectively. For the comparison between the simulation and Exp. (3), I_{sc} and P_{max} under T_h = 145 °C – T_c = 41 °C were 14.9 % and 0.7 % higher, respectively, while V_{oc} was 18.7 % lower. Lastly, comparing the simulation with Exp. (4), I_{sc} and P_{max} under T_h = 165 °C – T_c = 50 °C were 16.1 % and 0.6 % higher, respectively, while V_{oc} was 19.8 % lower.

While there are slightly larger differences between some simulations and experiments in terms of both I_{sc} and V_{oc} in certain cases, the disparity at the level of P_{max} does not exceed 1 % in all simulations. This could be due to the complexity of temperature distribution in experiments, making it challenging to accurately simulate all aspects. Therefore, our primary focus was on P_{max} rather than I_{sc} and V_{oc}.

The Root Mean Square Error (RMSE) was employed as a statistical measure to evaluate the agreement between simulation and experimental results across Cases 1–4. In Case 1, considering the simulation P_{max} results for the four concentration ratios and corresponding to the average temperatures measured on the hot side, the RMSE value was 0.505 (Fig. 8a). The dependence is linear, with a coefficient of determination equal to 0.9838. A substantial improvement in RMSE was observed when considering the best simulation P_{max} results obtained. Fig. 8b shows the P_{max} vs concentration ratio for the measured and best simulated points. The matching be-

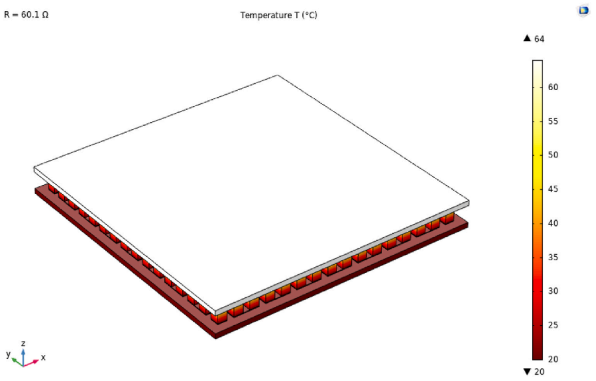

Fig. 5. Simulation of the TEG module under uniform temperatures on both the hot and cold sides (T_h = 64 °C – T_c = 20 °C).

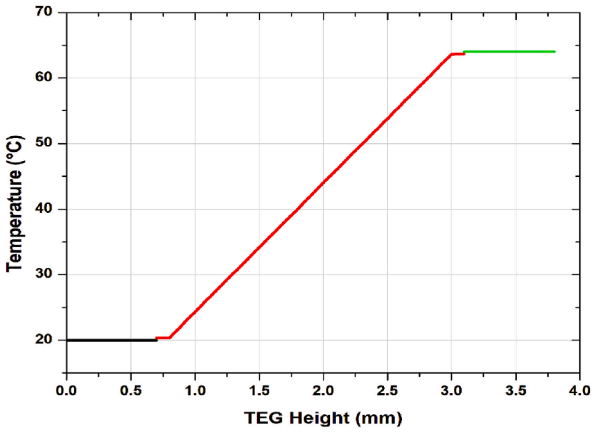

Fig. 6. Temperature variation across the TEG module under uniform temperatures on both the hot and cold sides (T_h = 64 °C – T_c = 20 °C).

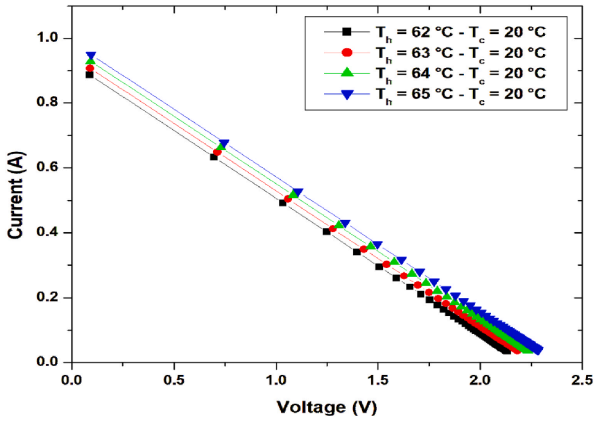

(a)

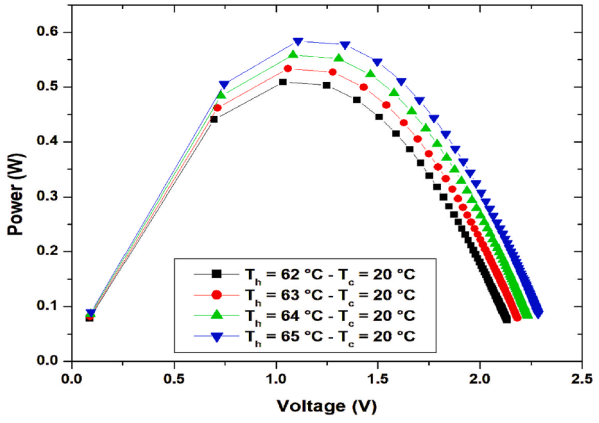

(b)

Fig. 7. The I–V and P–V characteristics of the TEG module simulated under different uniform temperatures on both the hot and cold sides with a) I–V characteristic and b) P–V characteristic.

tween experimental P_{max} results and simulation P_{max} ones was found to be very good (see Fig. 8b), and the calculated RMSE value being 0.017.

3.2.2. Case 2: nonuniform temperature on the hot side – uniform temperature on the cold side

In reality, the temperature distributions on the hot sides of TEG modules are not uniform. To better approximate real-world conditions, six patterns of nonuniform temperature distribution were proposed, consisting of three different circular and three different rectangular distributions. In the current case (Case 2), these six patterns of nonuniform temperature distribution were applied to the hot side of the TEG module for each high-concentration radiation scenario (i.e., Exp. (1)–(4)).

For example, in simulating Exp. (1), we proposed six circular and rectangular patterns of nonuniform temperature distribution, each with an average temperature of 64 °C, as determined in the previous case (Case 1). Additionally, simulations were conducted for each of these six patterns to determine which one closely matches the results of Exp. (1), thus providing a more accurate representation of reality. Figs. 9 and 10 depict the TEG module simulated with these six circular and rectangular patterns of nonuniform temperature distribution on its hot side, while maintaining uniform temperature on its cold side ($T_{h,av} = 64\ °C - T_c = 20\ °C$). Corresponding simulation results, including I_{sc}, V_{oc}, and P_{max}, are presented in Table 7.

According to the simulation results, two patterns of nonuniform temperature distribution closely matched those observed in Exp. (1): the 3rd circular pattern (see Fig. 9c) and the 3rd rectangular pattern (see Fig. 10c). The TEG module with the 3rd circular pattern exhibited slightly higher I_{sc} and P_{max} compared to Exp. (1) by 0.1 % and 0.4 %, respectively, while V_{oc} was 6.5 % lower. Similarly, the TEG module with the 3rd rectangular pattern also showed slightly higher I_{sc} and P_{max} compared to Exp. (1) by 1.7 % and 3.8 %, respectively, while V_{oc} was 5 % lower. Therefore, the simulation results obtained with the 3rd circular pattern were superior to those obtained with the 3rd rectangular pattern.

Table 6
I_{sc}, V_{oc}, and P_{max} generated by TEG module simulated under different uniform temperatures on both the hot and cold sides.

	T_h (°C)	$T_{h,av}$ (°C)	T_c (°C)	$T_{c,av}$ (°C)	I_{sc} (A)	V_{oc} (V)	P_{max} (W)
Exp. (1)	54.2; 70.7	62.4	20.2; 19.6	19.9	0.926	2.386	0.555
Simulation	62		20		0.886	2.132	0.509
	63		20		0.907	2.182	0.533
	64		20		0.928 (+0.2 %)	2.233 (−6.4 %)	0.559 (+0.7 %)
	65		20		0.949	2.284	0.584
Exp. (2)	92.1; 126.4	109.2	30.1; 30.6	30.3	1.539	4.690	1.807
Simulation	109		30		1.663 (+8.0 %)	4.009 (−14.5 %)	1.798 (−0.5 %)
	110		30		1.684	4.060	1.844
Exp. (3)	128.1; 175.6	151.8	39.9; 42.5	41.2	1.903	6.490	3.088
Simulation	144		41		2.166	5.227	3.052
	145		41		2.187 (+14.9 %)	5.277 (−18.7 %)	3.111 (+0.7 %)
	150		41		2.292	5.531	3.417
	151		41		2.313	5.582	3.479
	152		41		2.334	5.633	3.543
Exp. (4)	151.4; 205.5	178.4	47.2; 52.0	49.6	2.081	7.274	3.776
Simulation	160		50		2.311	5.582	3.477
	164		50		2.395	5.785	3.735
	165		50		2.416 (+16.1 %)	5.835 (−19.8 %)	3.800 (+0.6 %)
	170		50		2.521	6.089	4.137
	178		50		2.688	6.495	4.706
	179		50		2.709	6.546	4.780

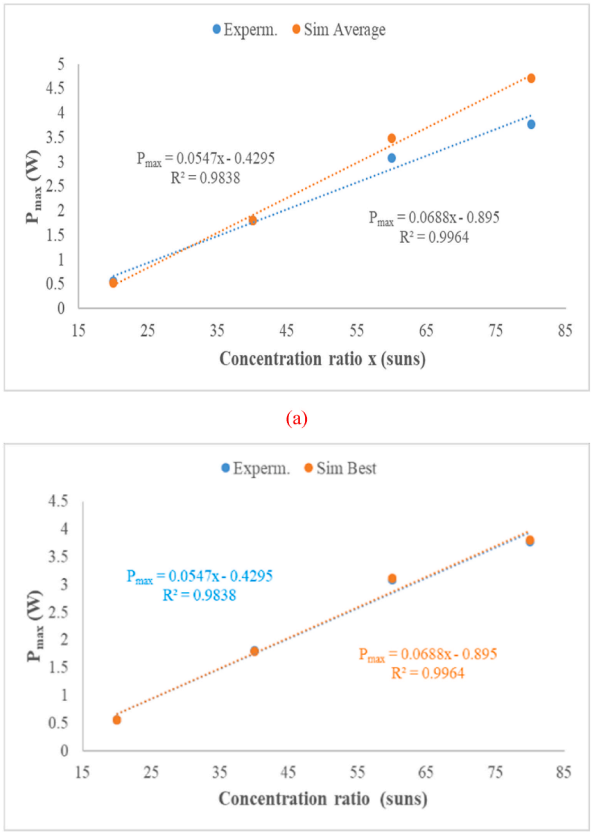

Fig. 8. Quantitative comparison of simulation and experimental P_{max} results in Case 1, showing a) measured and simulated P_{max}, b) measured and best simulated P_{max}.

Similarly, our six circular and rectangular patterns of nonuniform temperature distribution were employed in simulating Exp. (2)–(4), with the HS average temperature set to 109 °C for Exp. (2), 145 °C for Exp. (3), and 178 °C for Exp. (4). These HS average temperatures were determined through simulations conducted in the previous case (Case 1). Additionally, simulations were performed for each of the six patterns to identify which one yielded result closest to those of Exp. (2)–(4). Tables 8–10 present the corresponding

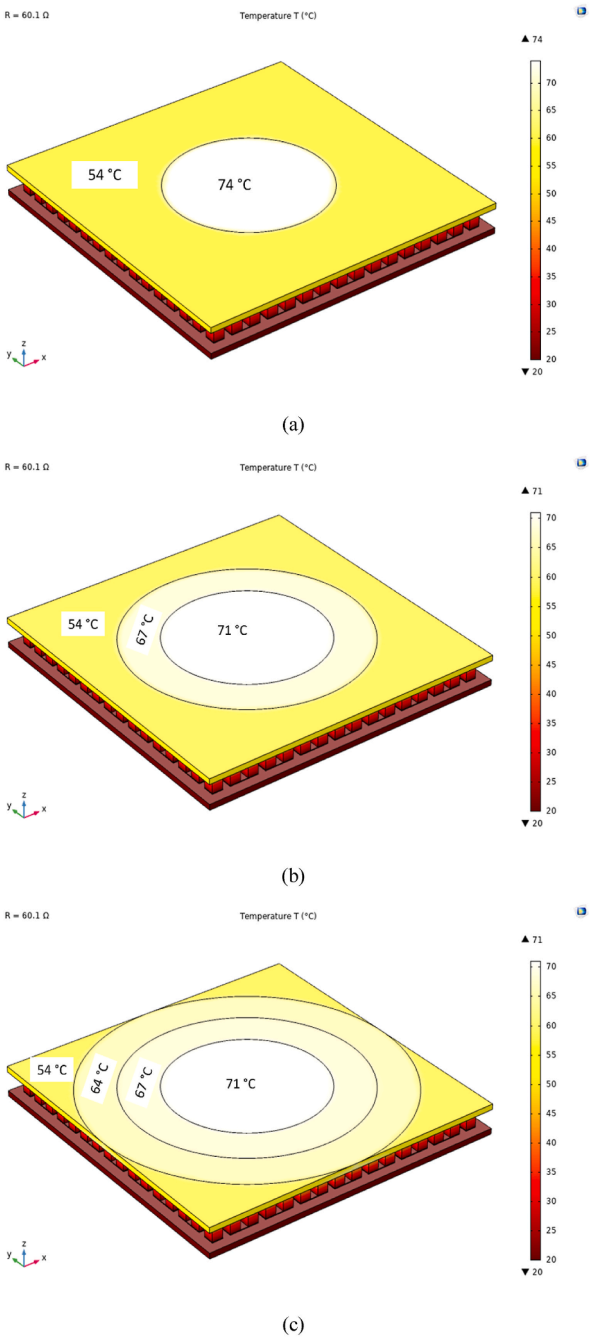

Fig. 9. Simulation of the TEG module with three different circular patterns of nonuniform temperature distribution on its hot side and uniform temperature on its cold side ($T_{h,av}$ = 64 °C – T_c = 20 °C).

simulation results, including I_{sc}, V_{oc}, and P_{max}, provided by the TEG module simulated with these six circular and rectangular patterns of nonuniform temperature distribution on its hot side while maintaining uniform temperatures on its cold side.

The behavior of the V_{oc}, I_{sc} and P_{max} when the hot side of TEG is split in more temperature zones is in concordance with the theory and several papers [37,39,41]. The Seebeck voltage is directly proportional with the difference of the temperature. In the 3rd circular or 3rd rectangular cases the number of p-n pairs for which the temperature difference is higher and the V_{oc} increases. The Seebeck coefficient is temperature dependent also. The current also increases when the temperature difference is higher due to the strongly vibration of the electrons from the hot side [39]. In consequence the P_{max} also increases. Comparing the current generated by TEG in the case of the uniform temperature distribution shows that it is higher than in the case of a nonuniform one, which is in concordance with the second law of thermodynamics.

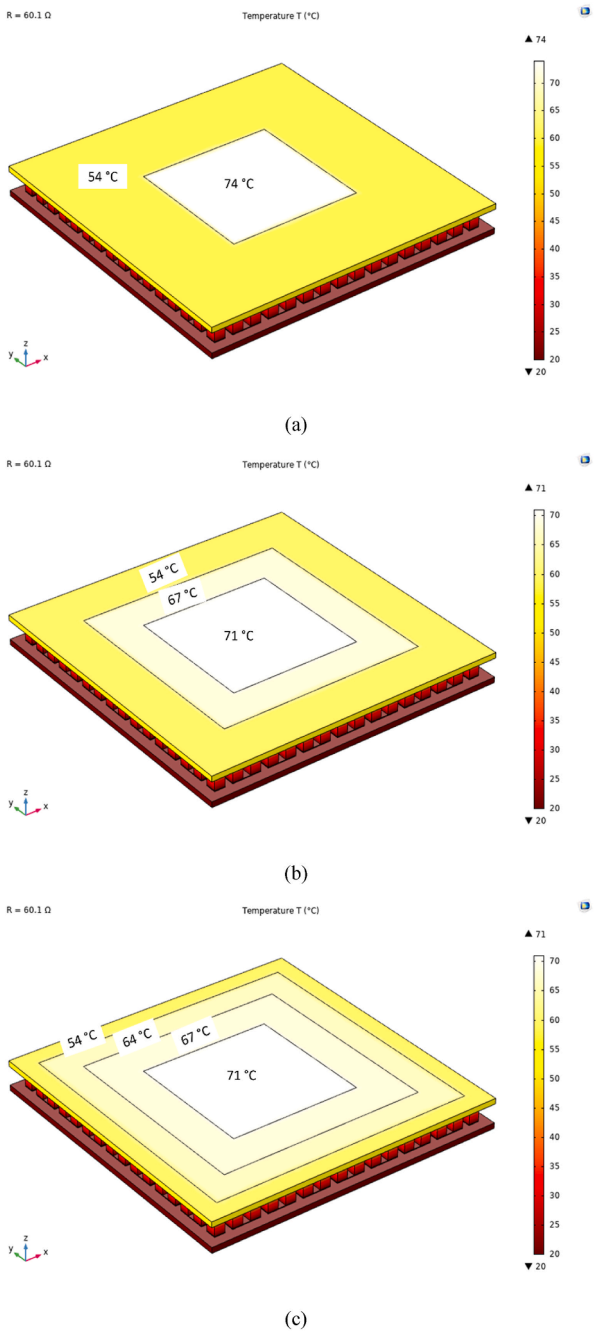

Fig. 10. Simulation of the TEG module with three different rectangular patterns of nonuniform temperature distribution on its hot side and uniform temperature on its cold side ($T_{h,av}$ = 64 °C – T_c = 20 °C).

Consistently, for Exps. (2) – (4), the 3rd circular and rectangular patterns of nonuniform temperature distribution yielded results closest to those of the corresponding experiments. Additionally, the simulation of the TEG module with the 3rd circular pattern better matched Exps. (2) and (4) compared to the 3rd rectangular pattern. Conversely, the 3rd rectangular pattern matched Exp. (3) more closely.

When comparing the P_{max} measured in Exp. (2), the TEG module with the 3rd circular pattern provided a P_{max} that was 0.1 % higher, while the 3rd rectangular pattern gave a 1.2 % higher P_{max}. For Exps. (3) and (4), the TEG module with the 3rd circular pattern showed a P_{max} that was 1.3 % lower and 1.0 % higher, respectively. Conversely, the TEG module with the 3rd rectangular pattern had a P_{max} 0.3 % lower for Exp. (3) and 1.6 % higher for Exp. (4).

Although the TEG module with the 3rd rectangular pattern yielded results closest to Exp. (3), the TEG module with the 3rd circular pattern still outperformed the 3rd rectangular pattern (3 times versus only once). Therefore, the 3rd circular pattern of nonuni-

Table 7
I_{sc}, V_{oc}, and P_{max} provided by the TEG module simulated with six circular and rectangular patterns of nonuniform temperature distribution on its hot side and uniform temperature on its cold side ($T_{h,av}$ = 64 °C – T_c = 20 °C).

	Pattern	T_h (°C)	$T_{h,av}$ (°C)	T_c (°C)	$T_{c,av}$ (°C)	I_{sc} (A)	V_{oc} (V)	P_{max} (W)
Exp. (1)		54.2; 70.7	62.4	20.2; 19.6	19.9	0.926	2.386	0.555
Simulation	Circ.	54; 74 (Fig. 9a)	64	20		0.807	1.941	0.422
		54; 67; 71 (Fig. 9b)	64	20		0.866	2.084	0.487
		54; 64; 67; 71 (Fig. 9c)	64	20		0.927 (+0.1 %)	2.231 (−6.5 %)	0.557 (+0.4 %)
	Rect.	54; 74 (Fig. 10a)	64	20		0.807	1.941	0.422
		54; 67; 71 (Fig. 10b)	64	20		0.878	2.112	0.500
		54; 64; 67; 71 (Fig. 10c)	64	20		0.942 (+1.7 %)	2.267 (−5.0 %)	0.576 (+3.8 %)

Table 8
I_{sc}, V_{oc}, and P_{max} provided by the TEG simulated with different nonuniform temperature circular and rectangular patterns on the hot side and uniform temperature on the cold side ($T_{h,av}$ = 109 °C – T_c = 30 °C).

	Pattern	T_h (°C)	$T_{h,av}$ (°C)	T_c (°C)	$T_{c,av}$ (°C)	I_{sc} (A)	V_{oc} (V)	P_{max} (W)
Exp. (2)		92.1; 126.4	109.2	30.1; 30.6	30.3	1.539	4.690	1.807
Simulation	Circ.	92; 126	109	30		1.458	3.513	1.381
		92; 109; 126	109	30		1.553	3.742	1.567
		92; 103; 115; 126	109	30		1.669 (+8.4 %)	4.022 (−14.2 %)	1.809 (+0.1 %)
	Rect.	92; 126	109	30		1.458	3.512	1.380
		92; 109; 126	109	30		1.568	3.778	1.597
		92; 103; 115; 126	109	30		1.677 (+8.9 %)	4.043 (−13.8 %)	1.828 (+1.2 %)

Table 9
I_{sc}, V_{oc}, and P_{max} provided by the TEG simulated with different nonuniform temperature circular and rectangular patterns on the hot side and uniform temperature on the cold side ($T_{h,av}$ = 145 °C – T_c = 41 °C).

	Pattern	T_h (°C)	$T_{h,av}$ (°C)	T_c (°C)	$T_{c,av}$ (°C)	I_{sc} (A)	V_{oc} (V)	P_{max} (W)
Exp. (3)		128.1; 175.6	151.8	39.9; 42.5	41.2	1.903	6.490	3.088
Simulation	Circ.	128; 162	145	41		1.982	4.782	2.555
		128; 132; 175	145	41		2.062	4.976	2.766
		128; 132; 145; 175	145	41		2.165 (+13.8 %)	5.224 (−19.5 %)	3.048 (−1.3 %)
	Rect.	128; 162	145	41		1.982	4.781	2.554
		128; 132; 175	145	41		2.065	4.983	2.774
		128; 132; 145; 175	145	41		2.175 (+14.3 %)	5.249 (−19.1 %)	3.077 (−0.3 %)

Table 10
I_{sc}, V_{oc}, and P_{max} provided by the TEG simulated with different nonuniform temperature circular and rectangular patterns on the hot side and uniform temperature on the cold side ($T_{h,av}$ = 165 °C – T_c = 50 °C).

	Pattern	T_h (°C)	$T_{h,av}$ (°C)	T_c (°C)	$T_{c,av}$ (°C)	I_{sc} (A)	V_{oc} (V)	P_{max} (W)
Exp. (4)		151.4; 205.2	178.4	47.2; 52	49.6	2.081	7.274	3.776
Simulation	Circ.	151; 179	165	50		2.248	5.427	3.288
		151; 165; 179	165	50		2.326	5.616	3.520
		151; 160; 170; 179	165	50		2.421 (+16.3 %)	5.846 (−19.6 %)	3.814 (+1.0 %)
	Rect.	151; 179	165	50		2.247	5.426	3.287
		151; 165; 179	165	50		2.338	5.645	3.557
		151; 160; 170; 179	165	50		2.428 (+16.6 %)	5.863 (−19.4 %)	3.836 (+1.6 %)

form temperature distribution aligns better with the experiments compared to the other circular and rectangular patterns. Additionally, this preference for the circular pattern can be explained. When TEG modules are subjected to concentrated solar energy, the temperature of their hot side surfaces tends to be higher at the center and gradually decreases towards the edges due to energy conduction [24,37]. This phenomenon leads to nonuniform circular temperature distribution of direct heat received by TEG modules on their hot sides [24,51].

From Table 7 to Table 10, a gradual increase in P_{max} from the 1st to the 3rd pattern for each type was observed. When these patterns were applied to the hot-side surface of the TEG module, an increase in the ratio of the top-side temperature of hot p-n pairs to the hot-side surface was noted. This increase led to a rise in the temperature difference across corresponding p-n pairs and, consequently, in the P_{max} of the TEG module.

3.2.3. Case 3: uniform temperature on the hot side – nonuniform temperature on the cold side

A homogeneous temperature distribution as a boundary condition, typically considered for the cold side, represents an ideal scenario. However, this condition may not accurately reflect many practical thermoelectric devices [41].

In the present case (Case 3), the effect of nonuniform temperature distribution at the level of a single TEG module was investigated. Similar to Case 2, the six circular and rectangular patterns of nonuniform temperature distribution were also applied to the cold side of the TEG module for each high-concentration radiation scenario (i.e., Exp. (1)–(4)). These nonuniform temperature distribution patterns have average temperatures of 20 °C in the simulation of Exp. (1), 30 °C for Exp. (2), 41 °C for Exp. (3), and 50 °C for Exp. (4). Tables 11–14 present the corresponding simulation results, including I_{sc}, V_{oc}, and P_{max}, provided by the TEG module with these six circular and rectangular nonuniform temperature patterns on its cold side, while maintaining uniform temperature on its hot side in the simulation of our experiments (i.e., T_h = 64 °C – $T_{c,av}$ = 20 °C, T_h = 109 °C – $T_{c,av}$ = 30 °C, T_h = 145 °C – $T_{c,av}$ = 41 °C, and T_h = 165 °C – $T_{c,av}$ = 50 °C).

From the simulation results, it is evident that the 3rd pattern of circular and rectangular nonuniform temperature distributions closely matched all experiments except for Exp. (2), where it was the 1st pattern that was the closest. Additionally, it is observed that the simulation results provided by the TEG module with the 3rd circular and rectangular nonuniform temperature patterns were identical.

Table 11
I_{sc}, V_{oc}, and P_{max} values generated by TEG under uniform temperature on its hot side while nonuniform temperature circular and rectangular patterns on its cold side (T_h = 64 °C – $T_{c,av}$ = 20 °C).

	Pattern	T_h (°C)	$T_{h,av}$ (°C)	T_c (°C)	$T_{c,av}$ (°C)	I_{sc} (A)	V_{oc} (V)	P_{max} (W)
Exp. (1)		54.2; 70.7	62.4	20.2; 19.6	19.9	0.926	2.386	0.555
Simulation	Circ.	64		19.6; 20.2	19.9	0.934	2.247	0.565
		64		19.6; 19.9; 20.2	19.9	0.932	2.243	0.563
		64		19.6; 19.8; 20; 20.2	19.9	0.930 (+0.4 %)	2.238 (−6.2 %)	0.561 (+1.1 %)
	Rect.	64		19.6; 20.2	19.9	0.934	2.247	0.566
		64		19.6; 19.9; 20.2	19.9	0.932	2.242	0.563
		64		19.6; 19.8; 20; 20.2	19.9	0.930 (+0.4 %)	2.238 (−6.2 %)	0.561 (+1.1 %)

Table 12
I_{sc}, V_{oc}, and P_{max} values generated by TEG under uniform temperature on its hot side while nonuniform temperature circular and rectangular patterns on its cold side (T_h = 109 °C – $T_{c,av}$ = 30 °C).

	Pattern	T_h (°C)	$T_{h,av}$ (°C)	T_c (°C)	$T_{c,av}$ (°C)	I_{sc} (A)	V_{oc} (V)	P_{max} (W)
Exp. (2)		92.1; 126.4	109.2	30.1; 30.6	30.3	1.539	4.690	1.807
Simulation	Circ.	109		30.1; 30.6	30.3	1.659 (+7.8 %)	3.999 (−14.7 %)	1.788 (−1.0 %)
		109		30.1; 30.3; 30.6	30.3	1.658	3.996	1.786
		109		30.1; 30.3; 30.4; 30.6	30.3	1.656	3.991	1.781
	Rect.	109		30.1; 30.6	30.3	1.659 (+7.8 %)	3.999 (−14.7 %)	1.788 (−1.0 %)
		109		30.1; 30.3; 30.6	30.3	1.658	3.996	1.786
		109		30.1; 30.3; 30.4; 30.6	30.3	1.656	3.991	1.782

Table 13
I_{sc}, V_{oc}, and P_{max} values generated by TEG under uniform temperature on its hot side while nonuniform temperature circular and rectangular patterns on its cold side (T_h = 145 °C – $T_{c,av}$ = 41 °C).

	Pattern	T_h (°C)	$T_{h,av}$ (°C)	T_c (°C)	$T_{c,av}$ (°C)	I_{sc} (A)	V_{oc} (V)	P_{max} (W)
Exp. (3)		128.1; 175.6	151.8	39.9; 42.5	41.2	1.903	6.490	3.088
Simulation	Circ.	145		39.9; 42.5	41.2	2.198	5.305	3.144
		145		39.9; 41.2; 42.5	41.2	2.191	5.288	3.123
		145		39.9; 40.9; 41.5; 42.5	41.2	2.182 (+14.7 %)	5.266 (−18.8 %)	3.097 (+0.3 %)
	Rect.	145		39.9; 42.5	41.2	2.199	5.306	3.144
		145		39.9; 41.2; 42.5	41.2	2.190	5.286	3.121
		145		39.9; 40.9; 41.5; 42.5	41.2	2.182 (+14.7 %)	5.265 (−18.9 %)	3.097 (+0.3 %)

Table 14
I_{sc}, V_{oc}, and P_{max} values generated by TEG under uniform temperature on its hot side while nonuniform temperature circular and rectangular patterns on its cold side (T_h = 165 °C – $T_{c,av}$ = 50 °C).

	Pattern	T_h (°C)	$T_{h,av}$ (°C)	T_c (°C)	$T_{c,av}$ (°C)	I_{sc} (A)	V_{oc} (V)	P_{max} (W)
Exp. (4)		151.4; 205.2	178.4	47.2; 52	49.6	2.081	7.274	3.776
Simulation	Circ.	165		47; 52	49.5	2.457	5.934	3.930
		165		47; 49.5; 52	49.5	2.443	5.900	3.885
		165		47; 49; 50; 52	49.5	2.425 (+16.5 %)	5.857 (−19.5 %)	3.829 (+1.4 %)
	Rect.	165		47; 52	49.5	2.457	5.934	3.931
		165		47; 49.5; 52	49.5	2.441	5.896	3.880
		165		47; 49; 50; 52	49.5	2.425 (+16.5 %)	5.857 (−19.5 %)	3.829 (+1.4 %)

In terms of P_{max} provided by the TEG module, the 3rd circular and rectangular nonuniform temperature patterns provided results closest to the experiments, being 1.1 % higher than Exp. (1), 0.3 % higher than Exp. (3), and 1.4 % higher than Exp. (4). For the 1st circular and rectangular nonuniform temperature patterns, P_{max} was 1.0 % lower than Exp. (2). Overall, these simulation results closely matched the experimental data, with the 3rd circular and rectangular nonuniform temperature patterns being dominant compared to the 1st circular and rectangular patterns (3 times versus only once).

Conversely in Case 2, from Table 11 to Table 14, a gradual decrease in P_{max} from the 1st to the 3rd pattern for each type was observed. Here, the patterns were applied to the cold-side surface of the TEG module. This caused a decrease in the ratio of the bottom-side temperature of cold p-n pairs to the cold-side surface, resulting in a decrease in the temperature difference across corresponding p-n pairs and, consequently, in the P_{max} of the TEG module.

3.2.4. *Case 4: nonuniform temperatures over hot and cold sides*

Typically, constant temperature boundary conditions are assumed for both the hot and cold sides in the simulation of TEG modules, which represent an idealized scenario. However, these boundary conditions often fail to accurately represent the spatial temperature nonuniformity achieved in multidimensional TEG modules [42].

In the present case (Case 4), the effect of nonuniform temperature distribution over both the hot and cold sides of a single TEG module was investigated. Consistent with previous Cases 2 and 3, the six circular and rectangular patterns of nonuniform temperature distribution were also applied to both the hot and cold sides of the TEG module for each high-concentration radiation scenario (i.e., Exp. (1)–(4)). These nonuniform temperature patterns have average temperatures equal to $T_{h,av} = 64$ °C and $T_{c,av} = 20$ °C for the hot and cold sides, respectively, to simulate Exp. (1); $T_{h,av} = 109$ °C – $T_{c,av} = 30$ °C for Exp. (2); $T_{h,av} = 145$ °C – $T_{c,av} = 41$ °C for Exp. (3); and $T_{h,av} = 165$ °C – $T_{c,av} = 50$ °C for Exp. (4). Tables 15–18 present the corresponding simulation results, including I_{sc}, V_{oc}, and P_{max}, provided by the TEG module under these circular and rectangular nonuniform temperature patterns over its hot and cold sides.

From the simulation results, the 3rd pattern of both circular and rectangular nonuniform temperature distribution closely matched Exps. (1)–(4). Additionally, both the circular and rectangular patterns matching experiments yielded nearly identical results. The circular pattern showed a slight advantage in the simulation of Exps. (1) and (4), while the rectangular pattern was slightly more accurate for Exps. (2) and (3).

Table 15
I_{sc}, V_{oc}, and P_{max} values provided by TEG under nonuniform temperature circular and rectangular patterns on their hot and cold sides ($T_{h,av}$ = 64 °C – $T_{c,av}$ = 20 °C).

	Pattern	T_h (°C)	$T_{h,av}$ (°C)	T_c (°C)	$T_{c,av}$ (°C)	I_{sc} (A)	V_{oc} (V)	P_{max} (W)
Exp. (1)		54.2; 70.7	62.4	20.2; 19.6	19.9	0.926	2.386	0.555
Simulation	Circ.	54; 74	64	19.6; 20.2	19.9	0.813	1.955	0.428
		54; 67; 71	64	19.6; 19.9; 20.2	19.9	0.870	2.094	0.491
		54; 64; 67; 71	64	19.6; 19.8; 20; 20.2	19.9	0.943 (+1.8 %)	2.270 (−4.8 %)	0.577 (+3.9 %)
	Rect.	54; 74	64	19.6; 20.2	19.9	0.807	1.941	0.422
		54; 67; 71	64	19.6; 19.9; 20.2	19.9	0.882	2.121	0.504
		54; 64; 67; 71	64	19.6; 19.8; 20; 20.2	19.9	0.944 (+1.9 %)	2.272 (−4.8 %)	0.578 (+4.1 %)

Table 16
I_{sc}, V_{oc}, and P_{max} values provided by TEG under nonuniform temperature circular and rectangular patterns on their hot and cold sides ($T_{h,av}$ = 109 °C – $T_{c,av}$ = 30 °C).

	Pattern	T_h (°C)	$T_{h,av}$ (°C)	T_c (°C)	$T_{c,av}$ (°C)	I_{sc} (A)	V_{oc} (V)	P_{max} (W)
Exp. (2)		92.1; 126.4	109.2	30.1; 30.6	30.3	1.539	4.690	1.807
Simulation	Circ.	92; 126	109	30.1; 30.6	30.3	1.454	3.503	1.373
		92; 109; 126	109	30.1; 30.3; 30.6	30.3	1.548	3.729	1.556
		92; 103; 115; 126	109	30.1; 30.3; 30.4; 30.6	30.3	1.661 (+7.9 %)	4.004 (−14.6 %)	1.793 (−0.8 %)
	Rect.	92; 126	109	30.1; 30.6	30.3	1.453	3.502	1.372
		92; 109; 126	109	30.1; 30.3; 30.6	30.3	1.562	3.765	1.586
		92; 103; 115; 126	109	30.1; 30.3; 30.4; 30.6	30.3	1.670 (+8.5 %)	4.025 (−14.6 %)	1.812 (+0.3 %)

Table 17
I_{sc}, V_{oc}, and P_{max} values generated by TEG under nonuniform temperature circular and rectangular patterns on their hot and cold sides ($T_{h,av}$ = 145 °C – $T_{c,av}$ = 41 °C).

	Pattern	T_h (°C)	$T_{h,av}$ (°C)	T_c (°C)	$T_{c,av}$ (°C)	I_{sc} (A)	V_{oc} (V)	P_{max} (W)
Exp. (3)		128.1; 175.6	151.8	39.9; 42.5	41.2	1.903	6.490	3.088
Simulation	Circ.	128; 162	145	39.9; 42.5	41.2	1.994	4.810	2.585
		128; 132; 175	145	39.9; 41.2; 42.5	41.2	2.067	4.986	2.778
		128; 132; 145; 175	145	39.9; 40.9; 41.5; 42.5	41.2	2.160 (+13.5 %)	5.212 (−19.7 %)	3.034 (−1.7 %)
	Rect.	128; 162	145	39.9; 42.5	41.2	1.993	4.809	2.584
		128; 132; 175	145	39.9; 41.2; 42.5	41.2	2.069	4.991	2.783
		128; 132; 145; 175	145	39.9; 40.9; 41.5; 42.5	41.2	2.170 (+14.0 %)	5.236 (−19.3 %)	3.063 (−0.8 %)

Table 18
I_{sc}, V_{oc}, and P_{max} values generated by TEG under nonuniform temperature circular and rectangular patterns on their hot and cold sides ($T_{h,av}$ = 165 °C – $T_{c,av}$ = 50 °C).

	Pattern	T_h (°C)	$T_{h,av}$ (°C)	T_c (°C)	$T_{c,av}$ (°C)	I_{sc} (A)	V_{oc} (V)	P_{max} (W)
Exp. (4)		151.4; 205.2	178.4	47.2; 52	49.6	2.081	7.274	3.776
Simulation	Circ.	151; 179	165	47; 52	49.5	2.289	5.526	3.409
		151; 165; 179	165	47; 49.5; 52	49.5	2.353	5.681	3.602
		151; 160; 170; 179	165	47; 49; 50; 52	49.5	2.430 (+16.8 %)	5.868 (−19.3 %)	3.843 (+1.8 %)
	Rect.	151; 179	165	47; 52	49.5	2.289	5.526	3.409
		151; 165; 179	165	47; 49.5; 52	49.5	2.363	5.706	3.634
		151; 160; 170; 179	165	47; 49; 50; 52	49.5	2.437 (+17.1 %)	5.885 (−19.1 %)	3.865 (+2.3 %)

From Table 15 to Table 18, a gradual increase in P_{max} from the 1st to the 3rd pattern for each type was observed. In this case, the patterns were applied to both the hot-side and cold-side surfaces, combining the effects observed in Cases 2 and 3. Given that the temperature variation on the hot-side surface is greater than that on the cold-side, the patterns had a more significant impact on the hot-side, leading to an increase in the P_{max} of the TEG module from the 1st to the 3rd pattern.

3.2.5. *Comparing different cases*

The comparison across the four cases focused on maximum power. When comparing the TEG-module simulation results in the four cases with Exp. (1), P_{max} was 0.7 % higher in Case 1, 0.4 % higher in Case 2 (3rd circular pattern), 1.1 % higher in Case 3 (both 3rd circular and rectangular patterns), and 3.9 % higher in Case 4 (3rd circular pattern), respectively. It appears that there is no significant difference between all cases and Exp. (1); however, Case 2 (3rd circular pattern) provided the closest results to Exp. (1) compared to the other cases (refer to Fig. 11).

Similarly, when comparing the TEG-module simulation results in the four cases with Exp. (2), P_{max} was 0.5 % lower in Case 1, 0.1 % higher in Case 2 (3rd circular pattern), 1.0 % lower in Case 3 (both 1st circular and rectangular patterns), and 0.3 % higher in Case 4 (3rd rectangular pattern), respectively. It seems that there is no significant difference between all cases and Exp. (2); however, Case 2 (3rd circular pattern) provided the closest results to Exp. (2) compared to the other cases (refer to Fig. 12).

Additionally, when comparing the TEG-module simulation results in the four cases with Exp. (3), P_{max} was 0.7 % higher in Case 1, 0.3 % lower in Case 2 (3rd rectangular pattern), 0.3 % higher in Case 3 (both 3rd circular and rectangular patterns), and 0.8 % lower in Case 4 (3rd rectangular pattern), respectively. It appears that there is no significant difference between all cases and Exp. (3); however, Case 2 (3rd rectangular pattern) and Case 3 (both 3rd circular and rectangular patterns) provided the closest results to Exp. (3) compared to the other cases (refer to Fig. 13).

When comparing the TEG-module simulation results in the four cases with Exp. (4), P_{max} was 0.6 % higher in Case 1, 1.0 % higher in Case 2 (3rd circular pattern), 1.4 % higher in Case 3 (both 3rd circular and rectangular patterns), and 1.8 % higher in Case 4 (3rd

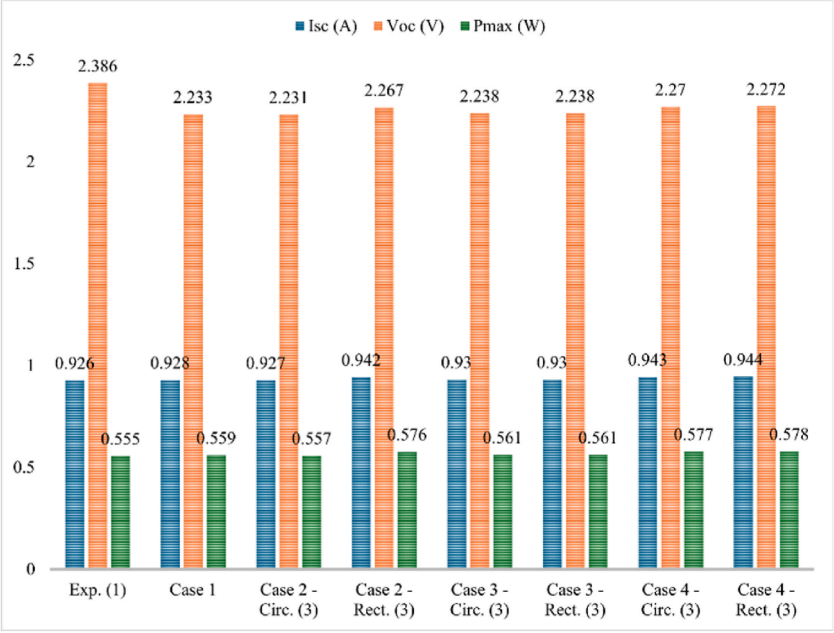

Fig. 11. Comparison of four cases in the simulation of Exp. (1).

Fig. 12. Comparison of four cases in the simulation of Exp. (2).

Fig. 13. Comparison of four cases in the simulation of Exp. (3).

circular pattern), respectively. Although there is no significant difference between all cases and Exp. (4), Case 1 provided the closest results to Exp. (4), followed by Case 2 (3rd circular pattern), compared to the other cases (refer to Fig. 14).

In tallying the number of matches for the 1st and 3rd circular and rectangular patterns, it was noticed that both the 3rd circular and rectangular patterns accurately simulated the experiments 11 times, whereas both the 1st circular and rectangular patterns succeeded only once (refer to Table 19).

When comparing the 3rd circular and 3rd rectangular patterns, the 3rd circular pattern exhibited a slight advantage in simulating Exps.(1), (2), and (4), while the 3rd rectangular pattern was slightly more accurate for Exp. (3) in Case 2. In Case 3, Both the 3rd circular and rectangular patterns showed similar advantages in simulating all experiments. In Case 4, Both the 3rd circular and rectangular patterns exhibited advantages equally.

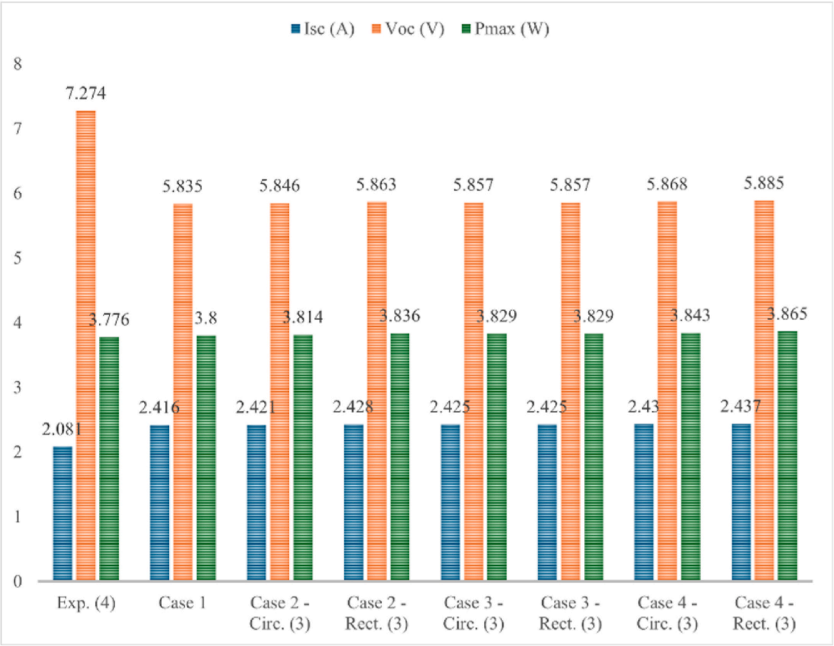

Fig. 14. Comparison of four cases in the simulation of Exp. (4).

Table 19
Comparison of the 1st and 3rd patterns of both circular and rectangular nonuniform temperature distribution.

	Number of simulation matches			
	Circular Pattern		Rectangular Pattern	
	1st	3rd	1st	3rd
Exp. (1)	0	3	0	3
Exp. (2)	1	2	1	2
Exp. (3)	0	3	0	3
Exp. (4)	0	3	0	3
Total	(01)	(11)	(01)	(11)

3.2.6. *Comparative study*

Table 20 displays a comparison of the power generation of TEG when the temperature is uniformly distributed on the hot side, versus when it is non-uniform. The temperature on the cold side of TEG is uniformly distributed for all cases considered. This comparison is made for two TEGs. In the case of the last TEG, six instances of non-uniformity are being considered. The uniform flux conduct at a non-uniformity in temperature distribution [24]. TEG from Ref. [24] has a loss in power of about 3.8 % in the case of strong temperature distribution non-uniformity. The simulations were achieved for the same temperatures as in the paper [24] to have a fair comparison [24]. The best matching between uniform and non-uniform temperature distribution is obtained for 2nd rectangular case. This can be happening due to TEG is a voltage source and the voltage generated is temperature-dependent, and be-

Table 20
Comparison between the uniform and nonuniform temperature distribution.

	HS Uniformity	Pattern		T_h (°C)	ΔT_h (°C)	T_c (°C)	P_{max} (W)	Nonuniformity Impact
Reference [24]	UHF	Square	Case 5	Between 177 and 206	29	25	4.65	–
	NUHF		Case 1	Between 172 and 218	46.2	25	4.5	−3.8 %
Current Study	UTD	–	–	191	–	25	7.918	–
	NUTD	Circular	1st	172; 218	46	25	7.065	−10.8 %
			2nd	172; 195; 218	46	25	7.625	−3.7 %
			3rd	172; 190; 200; 218	46	25	8.365	+5.6 %
		Rectangular	1st	172; 218	46	25	7.063	−10.8 %
			2nd	172; 195; 218	46	25	7.715	−2.5 %
			3rd	172; 190; 200; 218	46	25	8.390	+5.9 %

UHF – Uniform Heat Flux; NUHF – Non-Uniform Heat Flux; UTD – Uniform Temperature Distribution; NUTD – Non-Uniform Temperature Distribution.

cause the material properties are temperature-dependent. The configuration of the zones of the temperature distribution and their area can be another explanation [52].

4. Conclusion

Solar Thermoelectric Generators (STEG) have emerged as promising devices for clean energy production. However, nonuniform temperature distributions caused by optical concentrators and heat sinks on the hot and cold sides, respectively, can significantly impact their efficiency. Therefore, understanding temperature distribution on both sides of TEG modules is crucial for optimizing performance.

Previous studies mainly used central circles or identical squares to represent temperature nonuniformity. This paper investigates three circular and three rectangular patterns. Using COMSOL Multiphysics, TEG modules were simulated under four boundary conditions: (1) uniform temperature on both sides, (2) six circular and rectangular nonuniform temperature patterns on the hot side with uniform temperature on the cold side, (3) uniform temperature on the hot side with six circular and rectangular nonuniform temperature patterns on the cold side, and (4) six circular and rectangular nonuniform temperature patterns on both sides.

Numerical three-dimensional models of TEG modules with different patterns were constructed and simulated. The simulation results for each high-concentration radiation scenario were analyzed and compared with the experimental data. Simulations aligned well with all experiments under boundary condition (1). The 3rd pattern of both circular and rectangular matched 11 times, while the 1st pattern matched once under boundary conditions (2)–(4).

Comparing the 3rd circular and rectangular patterns, the 3rd circular pattern exhibited a slight advantage in simulating Exps.(1), (2), and (4), while the 3rd rectangular pattern was slightly more accurate for Exp. (3) under boundary condition (2). Under boundary condition (3), Both the 3rd circular and rectangular patterns showed similar advantages in simulating all experiments. under boundary condition (4), Both the 3rd circular and rectangular patterns exhibited advantages equally.

The Root Mean Square Error (RMSE) was employed as a statistical measure to estimate the agreement between simulation and experimental results across boundary conditions (1)–(4). The RMSE between the measured and simulated P_{max}, based on average measured temperatures on the hot side, was 0.505. For condition (1), the RMSE was 0.017, while for conditions (2) – (4), it was 0.027 (0.033), 0.031 (0.031), and 0.044 (0.047) for the 3rd circular (rectangular) pattern, respectively. These values indicate an improved alignment between the experimental and simulated results.

Future studies will focus on understanding temperature distribution in multi-layer TEG modules and exploring alternative patterns to further optimize performance.

CRediT authorship contribution statement

Abdelkader Rjafallah: Writing – review & editing, Writing – original draft, Visualization, Software, Methodology, Investigation, Formal analysis, Conceptualization. **Abubaker Younis:** Writing – review & editing. **Daniel Tudor Cotfas:** Writing – review & editing, Visualization, Validation, Supervision, Project administration, Methodology, Investigation, Formal analysis, Data curation, Conceptualization. **Petru Adrian Cotfas:** Visualization, Validation, Supervision, Project administration, Methodology, Investigation, Formal analysis, Data curation, Conceptualization.

Declaration of competing interest

The authors declare that they have no known competing financial interests or personal relationships that could have appeared to influence the work reported in this paper.

Data availability

Data will be made available on request.

Acknowledgments

The authors extend their appreciation to the Transilvania University of Brasov for funding this work through the Transilvania Fellowship for Postdoctoral Research/Young Researchers program.

References

[1] A. Ditta, A.N. Tabish, M.A. Mujtaba, M. Amjad, A.A. Yusuf, G.Q. Chaudhary, L. Razzaq, A. Abdelrahman, M.A. Kalam, Experimental investigation of a hybrid configuration of solar thermal collectors and desiccant indirect evaporative cooling system, Front. Energy Res. 10 (Sep. 2022).
[2] A. Younis, A. Rjafallah, P.A. Cotfas, D.T. Cotfas, Dust impact on electrical and thermal photovoltaic performance: insights from field and laboratory experiments, Energy Rep. 11 (Jun. 2024) 2099–2110.
[3] P.A. Cotfas, D.T. Cotfas, O.M. Machidon, Modelling and PSPICE simulation oi a photovoltaic/thermoelectric system, in: 2016 IEEE 22nd International Symposium for Design and Technology in Electronic Packaging (SIITME), 2016, pp. 179–183.
[4] REN21, Renewables 2019 Global Status Report, 2019.
[5] M. Farhan, M.I. Shahid, F. Jamil, M. Usman, M.A. Mujtaba, M.W. Saleem, S. Nasir Shah, S. Saghir, A.A. Yusuf, M. Mousa, A.S. El-Shafay, Performance evaluation of compound parabolic solar collector using different nanofluids: an experimental study, Front. Energy Res. 10 (Sep. 2022).
[6] P.A. Cotfas, D.T. Cotfas, Comprehensive review of methods and instruments for photovoltaic–thermoelectric generator hybrid system characterization, Energies 13 (22) (Jan. 2020) 6045.
[7] W. Zhou, X. Tang, J. Zhu, Design and optimal coolant flow rate analysis of an annular water-cooled automotive exhaust-based thermoelectric generator, Case Stud. Therm. Eng. 56 (Apr. 2024) 104256.

[8] M. Benghanem, A.A. Al-Mashraqi, K.O. Daffallah, Performance of solar cells using thermoelectric module in hot sites, Renew. Energy 89 (2016) 51–59.
[9] D. Champier, Thermoelectric generators: a review of applications, Energy Convers. Manag. 140 (2017) 167–181.
[10] A. Rjafallah, D.T. Cotfas, P.A. Cotfas, Legs geometry influence on the performance of the thermoelectric module, Sustainability 14 (23) (2022) 15823.
[11] D.T. Cotfas, A. Enesca, P.A. Cotfas, Enhancing the performance of the solar thermoelectric generator in unconcentrated and concentrated light, Renew. Energy 221 (Feb. 2024) 119831.
[12] D.T. Cotfas, P.A. Cotfas, Multiconcept methods to enhance photovoltaic system efficiency, Int. J. Photoenergy 2019 (Nov. 2019) e1905041.
[13] S.M. Pourkiaei, M.H. Ahmadi, M. Sadeghzadeh, S. Moosavi, F. Pourfayaz, L. Chen, M.A. Pour Yazdi, R. Kumar, Thermoelectric cooler and thermoelectric generator devices: a review of present and potential applications, modeling and materials, Energy 186 (2019) 115849.
[14] S. Shittu, G. Li, X. Zhao, X. Ma, Review of thermoelectric geometry and structure optimization for performance enhancement, Appl. Energy 268 (2020) 115075.
[15] Z. Ma, J. Wei, P. Song, M. Zhang, L. Yang, J. Ma, W. Liu, F. Yang, X. Wang, Review of experimental approaches for improving zT of thermoelectric materials, Mater. Sci. Semicond. Process. 121 (2021) 105303.
[16] K. Karthick, S. Suresh, M.M.M.D. Hussain, H.M. Ali, C.S.S. Kumar, Evaluation of solar thermal system configurations for thermoelectric generator applications: a critical review, Sol. Energy 188 (2019) 111–142.
[17] D.T. Cotfas, P.A. Cotfas, O.M. Machidon, D. Ciobanu, Investigation of the photovoltaic cell/thermoelectric element hybrid system performance, in: IOP Conf. Ser.: Mater. Sci. Eng., vol. 133, Jun. 2016, 012037 1.
[18] S. Mahmoudinezhad, A. Rezania, P.A. Cotfas, D.T. Cotfas, L.A. Rosendahl, Transient behavior of concentrated solar oxide thermoelectric generator, Energy 168 (Feb. 2019) 823–832.
[19] A.Z. Sahin, K.G. Ismaila, B.S. Yilbas, A. Al-Sharafi, A review on the performance of photovoltaic/thermoelectric hybrid generators, Int. J. Energy Res. 44 (5) (2020) 3365–3394.
[20] S. Shittu, G. Li, Y.G. Akhlaghi, X. Ma, X. Zhao, E. Ayodele, Advancements in thermoelectric generators for enhanced hybrid photovoltaic system performance, Renew. Sustain. Energy Rev. 109 (2019) 24–54.
[21] M. Gopinath, R. Marimuthu, Experimental study of photovoltaic-thermoelectric generator with graphite sheet, Case Stud. Therm. Eng. 54 (Feb. 2024) 103982.
[22] E. Yin, Q. Li, Y. Xuan, Effect of non-uniform illumination on performance of solar thermoelectric generators, Front. Energy 12 (2) (Jun. 2018) 239–248.
[23] S.A. Alsibiani, Experimental study of an optical concentrated solar thermoelectric power generator, Ain Shams Eng. J. 15 (2) (Feb. 2024) 102380.
[24] M. Ge, Z. Xuan, G. Zhang, Y. Zhao, Y. Zhao, Effect of non-uniform heat flux on solar thermoelectric generator, Energy Rep. 8 (Dec. 2022) 296–301.
[25] S. Ferreira-Teixeira, A.M. Pereira, Geometrical optimization of a thermoelectric device: numerical simulations, Energy Convers. Manag. 169 (Aug. 2018) 217–227.
[26] A. Fabián-Mijangos, G. Min, J. Alvarez-Quintana, Enhanced performance thermoelectric module having asymmetrical legs, Energy Convers. Manag. 148 (Sep. 2017) 1372–1381.
[27] Al Khalil, S. Sahnoun, A. Elhassnaoui, S. Yadir, A. Obbadi, Y. Errami, Solar thermoelectric generator and thermoelectric cooler performance: analysis and comparison using a different shape geometry, Clean Energy 7 (6) (Dec. 2023) 1233–1246.
[28] H.C. Luo, L.S. Cheng, Numerical study on optimizing the geometry of segmented asymmetrical thermoelectric generator, IOP Conf. Ser. Earth Environ. Sci. 701 (1) (Mar. 2021) 012022.
[29] Al Khalil, A. Elhassnaoui, S. Yadir, O. Abdellatif, Y. Errami, S. Sahnoun, Performance comparison of TEGs for diverse variable leg geometry with the same leg volume, Energy 224 (Jun. 2021) 119967.
[30] B. Şişik, S. LeBlanc, The influence of leg shape on thermoelectric performance under constant temperature and heat flux boundary conditions, Frontiers in Materials 7 (2020).
[31] H.-B. Liu, S.-L. Wang, Y.-R. Yang, W.-H. Chen, X.-D. Wang, Theoretical analysis of performance of variable cross-section thermoelectric generators: effects of shape factor and thermal boundary conditions, Energy 201 (Jun. 2020) 117660.
[32] Y. Thimont, S. LeBlanc, The impact of thermoelectric leg geometries on thermal resistance and power output, J. Appl. Phys. 126 (9) (Sep. 2019) 095101.
[33] S. Shittu, G. Li, X. Zhao, X. Ma, Y.G. Akhlaghi, E. Ayodele, Optimized high performance thermoelectric generator with combined segmented and asymmetrical legs under pulsed heat input power, J. Power Sources 428 (Jul. 2019) 53–66.
[34] A. Schönecker, B. Kraaijveld, A.E. van Til, A.J. Böttger, P. Brinks, M. Huijben, M. den Heijer, Cost efficient manufacturing of silicide thermoelectric materials and modules using RGS technique, Mater. Today: Proc. 2 (2) (Jan. 2015) 538–547.
[35] M. Chen, J. Zhang, L. Peng, Z. Dechang, Z. Lili, L. Rosendahl, T. Condra, Numerical and experimental optimization of thermoelectric modules for power generation: 6th European conference thermoelectrics, in: Proceedings of 6th European Conference Thermoelectrics, ECT 2008, 2008, pp. 1–22.
[36] A. Prasad, R.C. Thiagarajan, Multiphysics Modelling and Multilevel Optimization of Thermoelectric Generator for Waste Heat Recovery." presented at the COMSOL Conference 2018 Bangalore, ITC Gardenia, 2018.
[37] A. Lashin, M. Al Turkestani, M. Sabry, Performance of a thermoelectric generator partially illuminated with highly concentrated light, Energies 13 (14) (Jan. 2020) 3627.
[38] B.T. Admasu, X.B. Luo, J.W. Yao, T.Z. Ming, Effects of non-uniform hot junction temperature distribution on the outputs of thermoelectric power generation system, Appl. Mech. Mater. 283 (2013) 87–97.
[39] B.T. Admasu, X. Luo, J. Yao, Effects of temperature non-uniformity over the heat spreader on the outputs of thermoelectric power generation system, Energy Convers. Manag. 76 (Dec. 2013) 533–540.
[40] T. Ming, Q. Wang, K. Peng, Z. Cai, W. Yang, Y. Wu, T. Gong, The influence of non-uniform high heat flux on thermal stress of thermoelectric power generator, Energies 8 (11) (Nov. 2015) 12584–12602.
[41] B. Pfeiffelmann, C. Özman, A. Cemal Benim, F. Joos, Analysis of the effect of nonuniform surface temperature distribution on the performance of a thermoelectric generator, Sustain. Energy Technol. Assessments 53 (Oct. 2022) 102375.
[42] B. Pfeiffelmann, C. Özman, A.C. Benim, F. Joos, Variable temperature effects on TEG performance, in: E3S Web Conf., vol. 128, 2019 07004.
[43] S. Shittu, G. Li, Q. Xuan, X. Xiao, X. Zhao, X. Ma, Y.G. Akhlaghi, Transient and non-uniform heat flux effect on solar thermoelectric generator with phase change material, Appl. Therm. Eng. 173 (Jun. 2020) 115206.
[44] https://www.comsol.com.
[45] Y.J. Cui, K.F. Wang, B.L. Wang, J.E. Li, J.Y. Zhou, A comprehensive analysis of delamination and thermoelectric performance of thermoelectric pn-junctions with temperature-dependent material properties, Compos. Struct. 229 (Dec. 2019) 111484.
[46] D. Luo, Y. Zhao, J. Cao, W.-H. Chen, Y. Zhao, B. Cao, Performance analysis of a novel thermoelectric-based battery thermal management system, Renew. Energy 224 (Apr. 2024) 120193.
[47] D. Luo, Z. Wu, Y. Yan, J. Cao, X. Yang, Y. Zhao, B. Cao, Performance investigation and design optimization of a battery thermal management system with thermoelectric coolers and phase change materials, J. Clean. Prod. 434 (Jan. 2024) 139834.
[48] D. Luo, Z. Liu, Y. Yan, Y. Li, R. Wang, L. Zhang, X. Yang, Recent advances in modeling and simulation of thermoelectric power generation, Energy Convers. Manag. 273 (Dec. 2022) 116389.
[49] S. Mahmoudinezhad, A. Rezania, D.T. Cotfas, P.A. Cotfas, L.A. Rosendahl, Experimental and numerical investigation of hybrid concentrated photovoltaic – thermoelectric module under low solar concentration, Energy 159 (Sep. 2018) 1123–1131.
[50] J. Li, J. Gonzalez-Aguilar, C. Pérez-Rábago, H. Zeaiter, M. Romero, Optical analysis of a hexagonal 42kWe high-flux solar simulator, Energy Proc. 57 (Jan. 2014) 590–596.
[51] B. Yang, S. Wu, J. Huang, Z. Guo, J. Wang, Z. Zhang, R. Xie, H. Shu, L. Jiang, Salp swarm optimization algorithm based MPPT design for PV-TEG hybrid system under partial shading conditions, Energy Convers. Manag. 292 (Sep. 2023) 117410.
[52] A. Montecucco, J. Siviter, A.R. Knox, The effect of temperature mismatch on thermoelectric generators electrically connected in series and parallel, Appl. Energy 123 (Jun. 2014) 47–54.